iScience

CellPress
OPEN ACCESS

Article

Crowding and confinement act in concert to slow DNA diffusion within cell-sized droplets

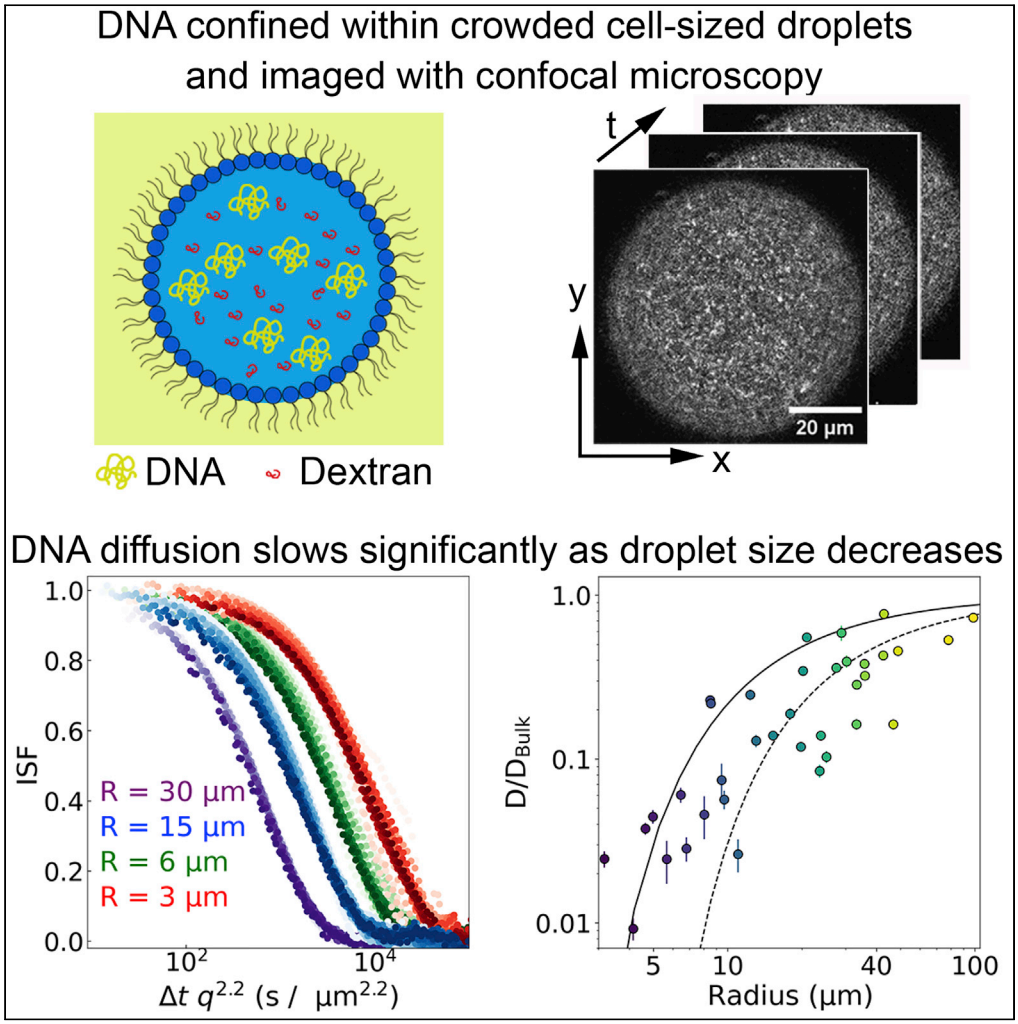

Mehdi Shafiei Aporvari, Steven Dang, Juexin Marfai, Kara Coursey, Ryan McGorty, Rae M. Robertson-Anderson

rmcgorty@sandiego.edu (R.M.)
randerson@sandiego.edu (R.M.R.-A.)

Highlights

DNA diffusion measured in cell-sized droplets with differential dynamic microscopy

Combination of crowding and confinement leads to subdiffusion and slowing

Diffusion coefficients of DNA decrease strongly with decreasing droplet size

Polymer scaling theories and depletion effects predict observed dynamics

Aporvari et al., iScience 25, 105122
October 21, 2022
https://doi.org/10.1016/j.isci.2022.105122

iScience

CellPress
OPEN ACCESS

Article

Crowding and confinement act in concert to slow DNA diffusion within cell-sized droplets

Mehdi Shafiei Aporvari,[1] Steven Dang,[1] Juexin Marfai,[1] Kara Coursey,[1] Ryan McGorty,[1,3,*] and Rae M. Robertson-Anderson[1,2,3,*]

SUMMARY

Dynamics of biological macromolecules, such as DNA, in crowded and confined environments are critical to understanding cellular processes such as transcription, infection, and replication. However, the combined effects of cellular confinement and crowding on macromolecular dynamics remain poorly understood. Here, we use differential dynamic microscopy to investigate the diffusion of large DNA molecules confined in cell-sized droplets and crowded by dextran polymers. We show that confined and crowded DNA molecules exhibit universal anomalous subdiffusion with scaling that is insensitive to the degree of confinement and crowding. However, effective DNA diffusion coefficients D_{eff} decrease up to 2 orders of magnitude as droplet size decreases—an effect that is enhanced by increased crowding. We mathematically model the coupling of crowding and confinement by combining polymer scaling theories with confinement-induced depletion effects. The generality and tunability of our system and models render them applicable to elucidating wide-ranging crowded and confined systems.

INTRODUCTION

A multitude of cellular processes depend on thermally driven dynamics—both center-of-mass transport and conformational fluctuations—of large macromolecules like DNA. Such transport dynamics strongly depend on the degree of crowding by other macromolecules and the degree of confinement by the cell membrane. These conditions, crowding and confinement, are common to intracellular spaces and their effects on transport have been extensively studied (McGuffee and Elcock, 2010; Zhou et al., 2008; Bucciarelli et al., 2016; Dix and Verkman, 2008). However, most studies investigating how crowding and confinement affect the diffusion of small particles or macromolecules have focused on *either* crowding *or* confinement (Balducci et al., 2006; Morrin et al., 2021; Hitimana et al., 2022; Bonthuis et al., 2008; Tan et al., 2013; Reisner et al., 2005; Skóra et al., 2020). How the interplay between crowding and confinement affects the transport of large macromolecules remains poorly understood.

Moreover, previous studies have largely used spherical colloidal particles or small molecules as tracers, rather than large macromolecules, since uniform and monodisperse suspensions of these materials can be easily obtained. However, both crowding and confinement have been shown to cause swelling or compaction of large macromolecules depending on the physical properties of the macromolecules and the environmental conditions (Kato et al., 2009; Jones et al., 2011; Junker et al., 2019; Gorczyca et al., 2015; Zhang et al., 2009). This important contribution to dynamics is missed in studies using nanoparticles, colloids, or small molecules. Here, to address this gap, we use large DNA tracers, which assume fluctuating random coil configurations in solution, and which we are able to produce with monodisperse controllable length and topology. Moreover, the use of DNA molecules more directly elucidates intracellular dynamics that are key to biological processes such as transformation, replication, and gene expression (Nakano et al., 2014; Weiss, 2014; Miyoshi and Sugimoto, 2008; Tan et al., 2013; Lukacs et al., 2000). Finally, we consider here the crowding regime in which the diffusing polymer tracers (DNA) are much larger than the crowding polymers (dextran), a very different regime than those typically examined both experimentally and theoretically in which the tracer polymer or particle is comparable to or smaller than the surrounding polymers (Guan et al., 2014; Kwon et al., 2014; Roosen-Runge et al., 2011). Specifically, the 115 kbp linear DNA polymers that we use have a coil size of $R_0 \approx 2\,\mu m$ compared to the ~16 nm hydrodynamic radius of the dextran random coils (Senti et al., 1955; Robertson et al., 2006; Armstrong et al., 2004). This >100 × mismatch between the DNA and dextran sizes ensures that the DNA is experiencing the bulk viscosity and

[1]Department of Physics and Biophysics, University of San Diego, 5998 Alcala Park, San Diego, CA 92110, USA

[2]Lead contact

[3]These authors contributed equally

*Correspondence: rmcgorty@sandiego.edu (R.M.), randerson@sandiego.edu (R.M.R.-A.)

https://doi.org/10.1016/j.isci.2022.105122

concentration of the dextran solution, rather than a lower effective viscosity that depends on the size ratio of the tracer and crowder (Kohli and Mukhopadhyay, 2012).

Macromolecular crowding can lead to anomalous thermal transport dynamics in which the mean squared displacement $\Delta r(\Delta t)^2$ does not increase linearly with lag time Δt, as is the case in normal Brownian diffusion in which $\Delta r(\Delta t)^2 \propto \Delta t^{\alpha}$ with $\alpha = 1$. Specifically, crowding can cause subdiffusion, described by $\Delta r(\Delta t)^2 \propto \Delta t^{\alpha}$ where $\alpha < 1$ is the anomalous scaling exponent (Höfling and Franosch, 2013; Metzler et al., 2016). Experiments examining diffusion in the crowded intracellular environment (Weiss et al., 2004; Banks and Fradin, 2005), as well as in *in vitro* crowding conditions (Junker et al., 2019; Skóra et al., 2020), have reported subdiffusive dynamics ($\alpha < 1$) with the deviation from normal diffusion (i.e., $\alpha = 1$) dependent on the concentration and type of crowders.

Similar to crowding, confinement has also been shown to slow the dynamics of particles and macromolecules (Balducci et al., 2006; Morrin et al., 2021). For example, previous studies have shown that the diffusion coefficient D of 36-nm-diameter particles decreased by ~20%–30% from its bulk value D_B when placed between surfaces separated by ~10 × the particle diameter. This slowdown was more pronounced as the degree of confinement increased (Hitimana et al., 2022). Several other studies that have reported similar slowing of particle diffusion near hard walls of confining slits, spheres, channels, and other geometries (Lin et al., 2000; Pawar and Anderson, 1993; Bevan and Prieve, 2000; Broersma, 1959; Zembrzycki et al., 2012; Kazoe and Yoda, 2011) have explained this slowing as arising from increased hydrodynamic drag near the surface. Ref (Behrens et al., 2003) approximates this reduced diffusion via the relation $D/D_B \simeq (6d^2 + 2\delta d)/(6d^2 + 9\delta d + 2\delta^2)$, where δ is the particle size and d is its distance from the confining wall (Behrens et al., 2003).

Several prior studies have also examined the dynamics of DNA molecules confined in nanoslits and nanochannels, focusing on the strong confinement regime where the confinement length scale is comparable to or smaller than the DNA coil size (Bonthuis et al., 2008; Tang et al., 2010; Reisner et al., 2005; Persson et al., 2009; Hitimana et al., 2022). Under these conditions, experiments and simulations have shown that DNA diffusion depends strongly on the degree of confinement, agreeing well with theoretical scaling relationships (De Gennes and Gennes, 1979; Morrin et al., 2021; Balducci et al., 2006; Chen et al., 2004). These studies shed light on the diffusion of DNA through pores and nanofluidic devices, yet their extension to weaker confinement conditions, both in terms of the size and softness of the confining vessel, as for DNA molecules within cells or intracellular compartments, is limited (Tang et al., 2010).

Few studies have probed the combined effects of crowding and confinement in the weak confinement regime (Jones et al., 2011). Recent studies using lipid-coated droplets to create a confining environment reported that diffusion coefficients of small molecules (~2–4 nm) in crowded environments decreased by a factor of ~2 compared to bulk values when confined in droplets of radius $R \approx 10$ μm (Watanabe et al., 2020). Follow-up work showed measurable decreases in molecular diffusivity in droplets with $R \approx 10 - 20$ μm, but only when the droplets contained $\gtrsim$ 20% (w/w) of 150 kDa dextran, with similar crowding by smaller molecules (glucose, 180 Da) having minimal effect (Harusawa et al., 2020). These studies reveal that even modest levels of confinement can significantly slow the thermal motion of molecules in crowded environments. However, a theoretical understanding of the observed slow diffusion under these conditions is lacking. Even less well understood is how the transport of large macromolecules is affected by similar levels of crowding and confinement.

Here, we investigate the dynamics of large DNA molecules in crowded and confined environments inspired by the intracellular environment. Specifically, we crowd 115 kbp DNA tracers, which have a coil size of $R_0 \approx 2$ μm, by smaller, highly overlapping dextran polymers with a hydrodynamic radius of $R_H \approx 16$ nm $> 100R_0$ and at concentrations >5-fold their overlap concentration c^*. We then confine this crowded system within isolated aqueous droplets coated with a lipid layer, and use differential dynamic microscopy (DDM) to measure the dynamics of the crowded and confined DNA molecules (Figure 1). DDM combines features of real-space image analysis and dynamic light scattering to quantify ensemble transport dynamics (Cerbino and Trappe, 2008; Cerbino et al., 2022). As DDM does not require real-space localization of molecules, it has been used in many previous studies where, due to highly overlapping molecules or poor signal to noise, particle tracking is not feasible (Regan et al., 2019; Drechsler et al., 2017; Feriani et al., 2017; Martinez et al., 2012; Lu et al., 2012). Using DDM, we show that the effective diffusion coefficients of DNA in

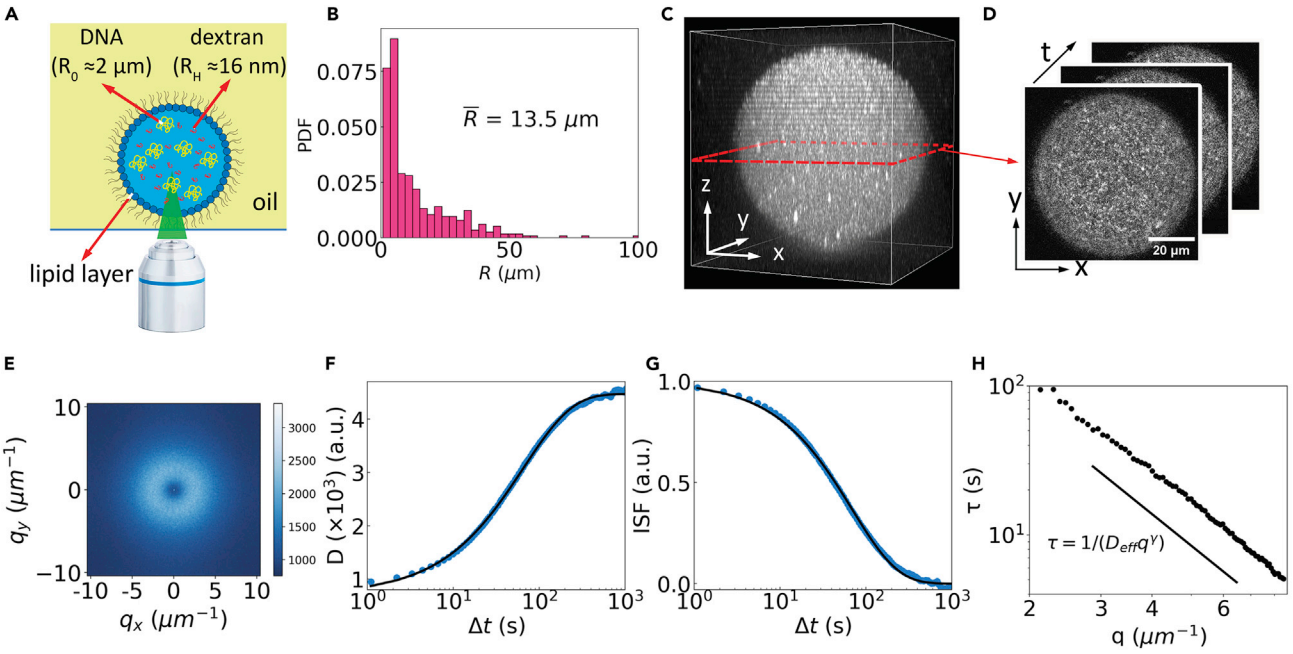

Figure 1. Experimental approach to investigating DNA diffusion subject to *in vitro* cell-mimicking crowding and confinement

(A) We use confocal fluorescence microscopy to measure the dynamics of 115 kbp DNA molecules ($R_0 \approx 2$ μm) diffusing in crowded solutions of 500 kDa dextran polymers ($R_H \approx 16$ nm) encapsulated in a droplet stabilized with a lipid layer within a continuous phase of mineral oil.

(B) The probability distribution of droplet radii R shows droplets with $R \simeq 3$ μm to ~ 100 μm and an average value of $\overline{R} \simeq 13.5$ μm.

(C) A 3D rendering of a focal stack of 39 images, 74 μm×74 μm in size, with a z-step size of 2.05 μm, shows the spherical shape of the droplets. The droplet shown has a radius of $R \simeq 37$ μm.

(D) A time series of images of DNA within the central plane of the droplet is used for DDM analysis.

(E–F) A representative 2D image structure function $D(q_x, q_y, \Delta t)$ for lag time $\Delta t = 6.6$ s is radially symmetric, indicating isotropic dynamics. Azimuthally averaging the 2D image structure functions for all lag times Δt results in 1D image structure functions $D(q, \Delta t)$, as shown for $q = 2.4\ \mu m^{-1}$ in (F). $D(q, \Delta t)$ versus Δt is well fit to the model in Equation 3 (black curve).

(G) The intermediate scattering function (ISF) as a function of Δt for $q = 2.4\ \mu m^{-1}$ decays from 1 to 0 and is fit to the model $f(q, \Delta t) = \exp(-(\Delta t/\tau(q))^{s(q)})$ (black curve).

(H) Decay time, $\tau(q)$, versus q shows power-law behavior described by $\tau(q) = 1/(D_{eff} q^{\gamma})$, which provides measures of the type and rate of macromolecular transport, via γ and D_{eff}, respectively. The data shown are for a droplet with radius $R \simeq 37$ μm and the scaling bar represents power-law scaling with $\gamma = 2.2$.

concentrated dextran solutions decrease by nearly two orders of magnitude when the radius of the confining droplet decreases from $R \simeq 100$ μm to ~ 5 μm, with the degree of slowing being substantially more pronounced at higher dextran concentration. To elucidate the physical mechanisms underlying the surprisingly large coupled effect of crowding and confinement on DNA dynamics, we combine scaling theories describing the dependence of polymer diffusion and coil size on concentration with depletion effects. The resulting mathematical model, which contains no free fitting parameters and is generally applicable to crowded and confined systems, captures the scaling of dynamics with droplet radius and degree of crowding remarkably well.

RESULTS

To probe the thermal motion of DNA molecules within crowded and confined environments, we create water-in-oil emulsions stabilized with a lipid mixture, resulting in lipid-coated aqueous droplets of radii $R \simeq 3 - 100$ μm with an average radius of $\overline{R} \simeq 13$ μm (see STAR Methods, Figures 1A and 1B). As shown in Figure 1C, we find that the droplets are spherical in shape and do not wet the hydrophobic glass surface.

To measure DNA dynamics, we use laser scanning confocal microscopy to image fluorescent-labeled 115 kbp DNA molecules in the central plane of the lipid-coated droplets (red square in Figure 1C), which contain varying concentrations of dextran ($c = 0\%, 14\%\ (w/w), 28\%\ \bullet (w/w)$). We measure the transport dynamics of the confined DNA by performing DDM analyses on time-series of images as described in STAR Methods (Figure 1D). With DDM, we find the characteristic decay time for density fluctuations $\tau(q)$ across a range of

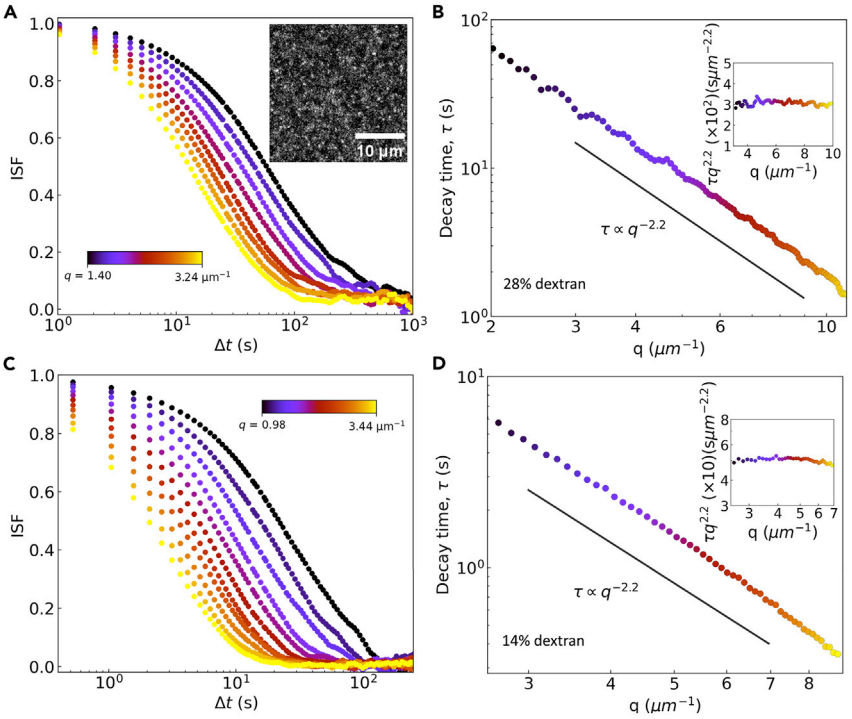

Figure 2. DDM analysis shows that large DNA molecules crowded by dextran polymers exhibit subdiffusive dynamics in bulk

(A) From DDM, we compute the ISFs across a range of wavevectors q for DNA in a bulk 28% (w/w) dextran solution. ISFs versus Δt for $= 1.40 - 3.24\ \mu m^{-1}$, indicated by the colorscale legend, are shown. Inset shows a representative 200× 200 pixel fluorescence confocal image of DNA molecules diffusing in a 28% dextran solution, which we use for DDM analysis.

(B) Decay time $\tau(q)$ versus q, determined from the ISFs shown in (A), exhibit power-law scaling behavior, $\tau(q) \propto q^{-\gamma}$ with $\gamma \simeq 2.2$, as shown by the solid black line. Inset shows the decay time scaled by $q^{2.2}$. The minimal q-dependence of $\tau q^{2.2}$ confirms that the dynamics are subdiffusive with an anomalous scaling exponent $\alpha = 2/\gamma \simeq 0.91$ over the entire range of examined lengthscales $\lambda = 2\pi/q \simeq 1.9\ \mu m - 4.5\ \mu m$.

(C) ISFs versus Δt computed for $q = 0.98 - 3.44\ \mu m^{-1}$ (indicated by colorscale) for DNA in a bulk 14% dextran solution show similar functional form as the decays shown in (A) but with a faster rate of decay.

(D) Decay time $\tau(q)$ versus q, determined from the ISFs shown in (C), exhibit power-law scaling with $\gamma \simeq 2.2$ (solid black line). Inset shows the decay time scaled by $q^{2.2}$. The scaling exponent is the same as that for 28% dextran (shown in A) but the magnitudes of $\tau(q)$ values are substantially lower, indicating faster dynamics.

wavevectors q. To do so, we first compute the image structure function, $D(q, \Delta t)$, by taking the Fourier transform of the differences of images separated by a given lag time, Δt, as described in STAR Methods. A representative slice of the image structure function for a particular lag time is shown in Figure 1E for DNA diffusing within a 37-μm-radius droplet. Computing image structure functions over a range of different lag times, Δt, allows us to determine how $D(q, \Delta t)$ varies with Δt for each q-value, as shown for $q = 2.4\ \mu m^{-1}$ in Figure 1F. By fitting $D(q, \Delta t)$ to the model described in Equation (3) (see STAR Methods), we compute the decay time $\tau(q)$ as a function of wavevector q. We also extract the ISF as a function of lag time, Δt, as shown for $q = 2.4\ \mu m^{-1}$ in Figure 1G. The decays of the ISFs and are well fit to the model $f(q, \Delta t) = \exp(-(\Delta t/\tau(q))^{s(q)})$ as shown by the black curve in Figure 1G. By determining the power law relationship between τ and q, i.e., $\tau(q) \propto q^{-\gamma}$, we determine the type of thermal transport (Figure 1H). Specifically, the scaling exponent γ reveals whether the dynamics are diffusive ($\gamma = 2$), subdiffusive ($\gamma > 2$), or superdiffusive ($\gamma < 2$).

Using this approach (Figure 1), we first consider how DNA dynamics are affected by crowding alone, without confinement, by measuring the transport of DNA in a bulk solution of 28% dextran (Figure 2). Our DDM analyses reveal that the DNA molecules move subdiffusively in this crowded dextran solution. We compute the ISFs for different wavevectors (Figure 2A) from which we determine $\tau(q)$ (Figure 2B). We find that $\tau(q)$ is well described by the power law relationship $\tau(q) = (D_{eff}\, q^{\gamma})^{-1}$, where D_{eff} is the effective diffusion coefficient, and $\gamma = 2.2$ is indicative of subdiffusive dynamics. Note that the parameter γ is

related to the scaling exponent, α, in the equation relating mean squared displacement to lag time (i.e., $\Delta r(t)^2 \sim t^{\alpha}$) by $\gamma = 2/\alpha$. Therefore, our data correspond to an anomalous exponent of $\alpha = 0.91$, in agreement with the previously reported value for the same DNA diffusing in a similar dextran solution (Harusawa et al., 2020). To better show the agreement of $\tau(q)$ with the subdiffusive power-law scaling $\gamma = 2.2$, we plot $\tau(q)$ scaled by $q^{2.2}$ (Figure 2B inset). As can be seen, $\tau q^{2.2}$ remains constant over the entire q range, confirming the scaling power of $\gamma = 2.2$.

As crowder concentration has been shown to play an important role in DNA dynamics (Zhou, 2013; Junker et al., 2019; Konopka et al., 2006; Elowitz et al., 1999), we compare our results for 28% dextran (Figures 2A and 2B) to those performed at 14% dextran (Figures 2C and 2D). We find that the ISFs for 14% dextran show similar functional form to the ISFs for 28% dextran (shown in Figure 2A), but the timescales over which the ISFs decay to 0 are shorter, indicating faster dynamics. Likewise, the corresponding decay time $\tau(q)$ is shorter for all q values (Figure 2D), another marker of faster mobility in the 14% dextran compared to 28%. However, surprisingly, the subdiffusive scaling exponent is unchanged by the reduction in dextran concentration. Namely, the power-law scaling of $\tau(q)$ for the 14% dextran is best described by $\gamma = 2.2$, just as for 28% dextran (Figure 2D inset).

While there are many mechanisms that can lead to subdiffusive dynamics in crowded systems (Polanowski and Sikorski, 2016; Höfling and Franosch, 2013; Golding and Cox, 2006; Kwon et al., 2014), the subdiffusion we measure here is likely a result of the viscoelasticity of the highly overlapping dextran solutions. Indeed, several previous studies have shown that the subdiffusion that tracers in high-concentration dextran solutions exhibit, with similarly modest exponents ($0.8 < \alpha < 1$), can be explained by the fractional Brownian motion model in which the viscoelasticity of the crowding medium results in the Brownian "steps" of the random walk not being completely independent (Banks and Fradin, 2005; Szymanski and Weiss, 2009; He et al., 2008). Moreover, previous studies have reported that dextran solutions exhibit viscoelastic properties at concentrations $\gtrsim$ 10% which are markedly increased for $\gtrsim$ 15% due to entanglements between the dextran molecules (McCurdy et al., 1994; Pinder et al., 2006). Reported signatures of viscoelasticity and entanglements included viscosity shear thinning and an elastic modulus greater than the viscous modulus (i.e., $G' > G''$) (Chapman et al., 2015; Pinder et al., 2006).

Because the dextran molecules are substantially smaller and thus more mobile than the DNA, we do not expect caging or obstructed diffusion of the DNA to play a role in the dynamics (Banks and Fradin, 2005). Moreover, our data show no signs of spatial heterogeneity, another potential source of anomalous diffusion, and previous studies examining similar crowding conditions in bulk likewise reported spatially homogeneous solutions (Chapman et al., 2015; Gorczyca et al., 2015).

Next, to determine how confinement alone, without crowding, affects DNA diffusion, we measure DNA dynamics inside aqueous lipid-coated droplets with no dextran (Figure 3). Unlike in crowded conditions, we find that the dynamics of the confined DNA are well described by normal Brownian diffusion for all droplet sizes ($R \simeq 6 - 84$ μm) as shown by the relatively constant values of τq^2 versus q for all R (Figure 3A). However, a clear dependence on droplet size is evident, with the scaled decay time τq^2 increasing as R decreases (denoted by the color gradient in Figure 3A). For the largest droplets, τq^2 is close to bulk values (black squares in Figure 3A), but as R decreases, this scaled decay time increases $\sim$3-fold. The corresponding diffusion coefficients, $D = \langle 1/\tau q^2 \rangle$ where <> represents the average over q, similarly decrease with decreasing droplet size as shown in Figure 3B. For the largest droplets ($R \gtrsim 80$ μm), D is similar to the bulk value D_B (dashed black line in Figure 3B), but as the droplet size decreases to $R \simeq 6$ μm the diffusion coefficient drops $\sim$3-fold. While decreasing DNA diffusion coefficients with increasing confinement have been noted in many prior studies (Balducci et al., 2006; Morrin et al., 2021; Bonthuis et al., 2008; Tang et al., 2010; Reisner et al., 2005; Persson et al., 2009), most have employed a strong degree of confinement where the confining length scale is comparable to or smaller than the DNA coil size R_0. Here, we observe a factor of $\sim$3 slowdown of the dynamics when the droplet radius is several times larger than R_0 ($\simeq 2$ μm).

The results discussed above show that crowding leads to subdiffusive DNA dynamics with effective diffusion coefficients that decrease with increasing crowding but with a scaling exponent that is insensitive to crowder concentration. Confinement, on the other hand, does not induce subdiffusion, but it does cause a slowing of DNA diffusion as the degree of confinement increases.

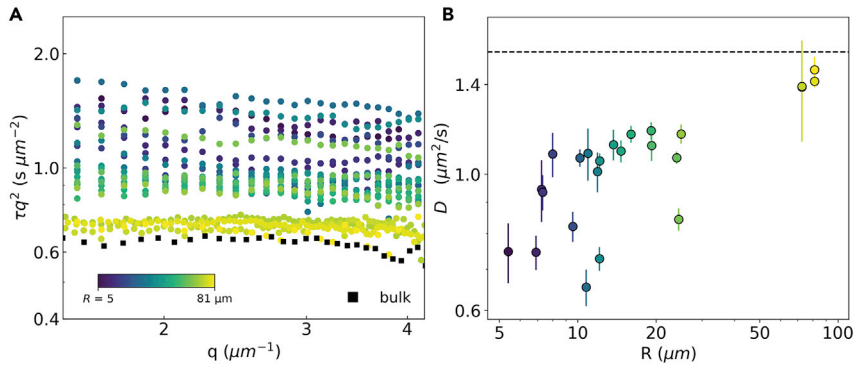

Figure 3. Confinement by cell-sized droplets slows the Brownian diffusion of large DNA molecules

(A) DDM decay times $\tau(q)$, scaled by q^2 and plotted versus q, for droplets with radii $R \simeq 6$ μm to $R \simeq 84$ μm, indicated by the colorscale legend, show no systematic dependence on q for all R values, indicating normal Brownian diffusion in which $\tau(q) \propto q^{-2}$.

(B) DNA diffusion coefficients are computed from the data shown in (A) via the relation $D = (\tau q^2)^{-1}$ and plotted as a function of droplet radius R. D is reduced nearly ~3-fold from the bulk value D_B (dashed horizontal line) as R decreases to ~ 6 μm. Error bars represent the standard deviation of the distribution of individual $D(q)$ values computed for each q value.

We now turn to understanding how these two different effects act in concert to dictate the dynamics of DNA that is both crowded and confined. For the data shown in Figure 4, we confine DNA molecules within lipid-coated droplets (as in Figure 3) that contain either 14% or 28% dextran (the solutions examined in Figure 2). Representative images of DNA within such droplets are shown in Figures 4A–4C. Using the same DDM analysis described above, we determine how the decay time $\tau(q)$ varies with q and R. Interestingly, we find that, similar to DNA molecules crowded by bulk dextran solutions (Figure 3), crowded DNA molecules confined within droplets exhibit subdiffusive dynamics with the same scaling exponent $\gamma = 2.2$ (Figures 4D and 4E). As can be seen in Figures 4D and 4E, where the scaled decay time $\tau q^{2.2}$ is plotted versus q for droplets of differing radii R, we observe minimal q dependence of $\tau q^{2.2}$ over the entire range of q and R values. (For comparison, the results for DNA in bulk dextran solutions (Figure 2) are shown with black squares.) Therefore, the degree to which the dynamics of crowded DNA are subdiffusive appears to be independent of the confinement size, at least for droplets with radii $R \gtrsim 3$ μm, as well as the degree of crowding (14 vs 28%).

To corroborate this finding, we also examine the stretching exponent $s(q)$ determined from fitting the DDM image structure function $D(q, \Delta t)$ (see STAR Methods). This stretching exponent is predicted to be comparable to the anomalous scaling exponent α (Guo et al., 2012; Jacob et al., 2015). Supplementary information Figure S1, which plots $s(q)$ for all R and q values for each dextran concentration shows that $s(q)$ is largely independent of R and q for both 14% and 28% dextran, with average values of $s = 0.83 \pm 0.02$ and $s = 0.86 \pm 0.02$, respectively. The consistency between s and α further verifies the subdiffusive nature of the dynamics we measure (Jacob et al., 2015).

We also note that $\tau(q)$ is noisy at small q for small droplets, which we understand as follows. The dynamics at small q values correspond to density fluctuations over large length scales, λ, i.e., $q = 2\pi/\lambda$. For example, $q = 3$ μm^{-1} corresponds to $\lambda \simeq 2$ μm which is not much smaller than the smallest droplet size. Therefore, in the limit of low q values, we expect noisier measurements of $\tau(q)$ for small droplets.

Interestingly, while the degree of subdiffusivity appears insensitive to confinement size and crowder concentration (Figures 4D and 4E), we observe a clear dependence of the effective diffusion coefficient, $D_{eff} = (\tau q^{2.2})^{-1}$, on droplet size that is more pronounced with increased crowding. This strong dependency of D_{eff} on droplet size within crowded environments can be clearly seen in Figures 4F and 4G where we have plotted D_{eff} versus droplet radius R.

As shown, when DNA is crowded by 28% dextran, D_{eff} in the smallest droplet ($R \simeq 4$ μm) is more than an order of magnitude slower than that measured in the bulk 28% dextran solution (Figure 4F). This drop in D_{eff} with decreasing droplet size R is also evident at the lower dextran concentration (14%), but the

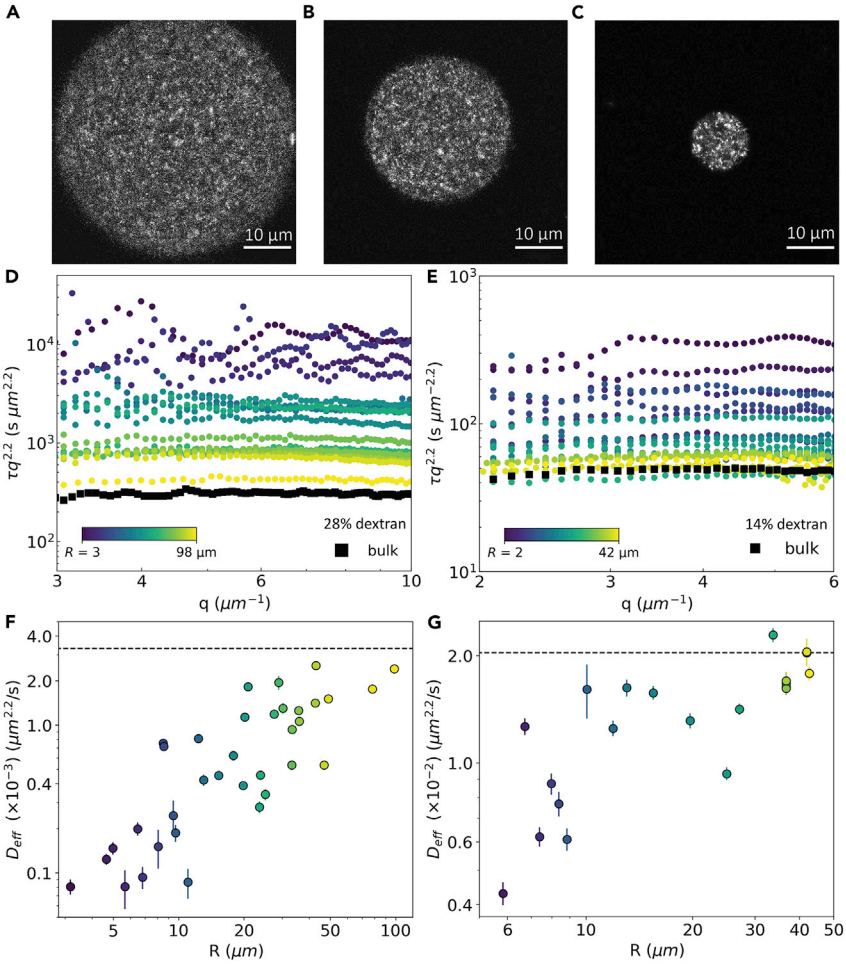

Figure 4. The coupled effects of confinement and crowding markedly slow the transport of DNA as droplet size decreases

(A–C) Confocal fluorescence images (512 × 512 pixel) of DNA molecules inside droplets of radii (A) $R \simeq 27$ μm, (B) $R \simeq 16$ μm, and (C) $R \simeq 6.2$ μm.

(D and E) Scaled decay times, $\tau q^{2.2}$, versus q for different droplet sizes, indicated by the colorscale legend, show that both 28% (D) and 14% (E) dextran solutions result in subdiffusive dynamics with the same scaling power of $\gamma \simeq 2.2$.

(F and G) Effective diffusion coefficients of confined DNA molecules, computed via the relation $D_{eff} = (\tau q^{2.2})^{-1}$, when crowded by 28% (F) and 14% (G) dextran solutions in droplets of varying radii R show a strong dependence on droplet size. The slowdown of DNA dynamics as droplet size decreases is most pronounced in the 28% dextran solution. Error bars represent the standard deviation of the distribution of individual $D(q)$ values computed for each q value.

decrease is less pronounced, with D_{eff} decreasing by up to a factor of ~5 from the bulk value when the droplet radius is lowered to $R \simeq 3$ μm (Figure 4G).

To confirm that our results are not biased by how we fit the image structure function, $D(q, \Delta t)$, that we obtain from DDM, we also compute the intermediate scattering functions (ISF) without fitting the data to a particular model, as described in STAR Methods. Figures 5A and 5B show the ISFs versus lag time, Δt, for DNA crowded by 28% dextran in droplets of $R \simeq 6.5$ μm (Figure 5A) and $R \simeq 30$ μm (Figure 5B) for a range of q values. As expected for ergodic systems, the ISFs decrease from 1 to 0 with decay rates that decrease with decreasing q values (increasing length scales λ). By rescaling Δt by $q^{2.2}$, we observe a collapse of the ISFs across the entire q range (Figures 5C and 5D). Recall that for normal Brownian diffusion, the characteristic decay time of the ISF varies with the wavevector as $\tau(q) \sim q^{-2}$. In such cases of normal diffusion, the q-dependent ISFs should collapse if plotted against $q^2 \Delta t$. Likewise, the collapse of the

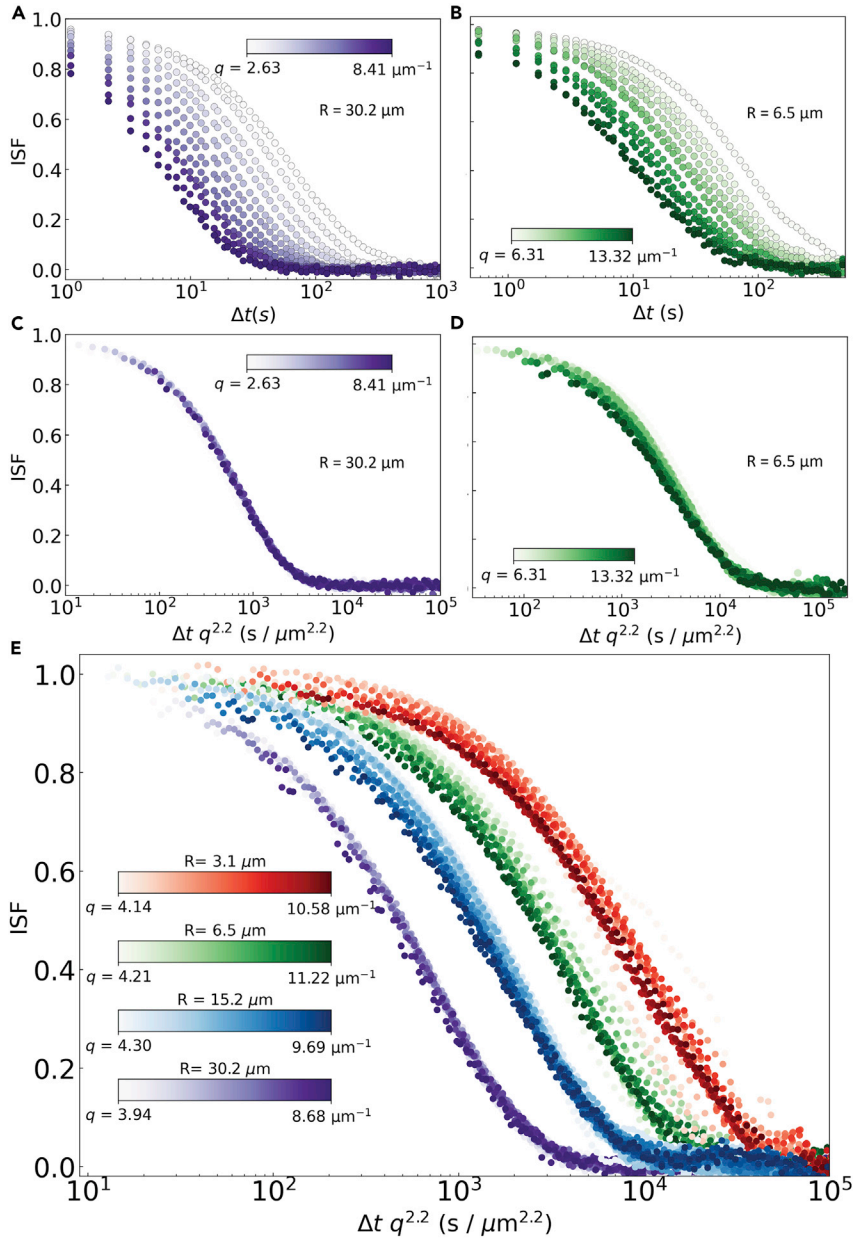

Figure 5. Collapse of ISFs reveal subdiffusive dynamics of large DNA molecules in crowded and confined environments

(A and B) ISFs versus lag time Δt for DNA diffusing in 28% dextran and confined in large ($R \simeq 30$ μm, A) and small ($R \simeq 6.5$ μm, B) droplets show decays at faster rates (smaller lag times Δt) as q increases.

(C and D) The ISFs shown in (A) (purple) and (B) (green) plotted as a function of a lag time scaled by $q^{2.2}$ (i.e., $q^{2.2}\Delta t$) collapse to a single curve, indicating the universality of the subdiffusive scaling $\gamma = 2.2$ across lengthscales.

(E) ISFs for DNA in 28% dextran and confined in droplets with $R \simeq 3.1$ μm (red), 6.5 μm (green), 15.2 μm (blue), and 30.2 μm (purple) all collapse when Δt is scaled by $q^{2.2}$. The collapsed ISFs decay more slowly for smaller droplets, indicating that confinement slows DNA diffusion.

ISFs when plotted versus $q^{2.2}\Delta t$ is consistent with our results showing $\tau(q) \sim q^{-2.2}$ (Figures 2B, 4D and 4E), as well as prior work showing that DNA in crowded dextran environments exhibits subdiffusive dynamics (Harusawa et al., 2020; Szymanski and Weiss, 2009).

To determine the robustness of this model-free data collapse to changing droplet size, we plot the ISFs versus $q^{2.2}\Delta t$ for four droplets of various sizes from $R \simeq 3$ μm to ~ 30 μm. As shown in Figure 5E, the ISFs collapse for all droplet sizes, indicating the invariance of the subdiffusive scaling to varying confinement size. Furthermore, the collapsed ISFs for the smallest droplet shown take an order of magnitude longer to decay than those for the largest droplet shown, consistent with the scaling of the effective diffusion coefficients of DNA with R (Figure 4F). Notably, while $\tau(q)$ and D_{eff} values presented in Figure 4 required fitting $D(q, \Delta t)$ to a particular model, we determine the ISFs presented in Figure 5 without any fitting or assumptions regarding the most appropriate model to describe the data.

DISCUSSION

The compounding effects of crowding and confinement—leading to a decrease in diffusivity with decreasing droplet size that is more pronounced with crowders than without—have indeed been noted in previous studies (Jones et al., 2011; Watanabe et al., 2020; Harusawa et al., 2020) For example, the diffusion coefficients of 1.7-nm-diameter fluorescent molecules within lipid-coated aqueous droplets were reported to decrease as the droplet size decreased from $R \simeq 20$ μm to $R \simeq 10$ μm. However, this R dependence was only seen for dextran concentrations of 23% and 29%, with no R dependence reported for concentrations $\leq$17% (Harusawa et al., 2020). Other studies have also reported on the combined effects of both crowding and confinement, though most focused on strongly confining slit-like or channel-like geometries (Balducci et al., 2006; Morrin et al., 2021; Tang et al., 2010; Reisner et al., 2005; Persson et al., 2009; Bonthuis et al., 2008) which are far from the weaker cell-like confinement we explore here.

Our collective results demonstrate that both crowding and confinement play important roles in the diffusion of DNA, both contributing to suppressing DNA mobility in distinct ways. Figures 3B, 4F, and 4G clearly show that increased confinement slows DNA diffusion. However, the extent to which DNA diffusion is hampered by confinement increases with increasing crowding, and the functional form of this decrease varies.

To elucidate the physical mechanisms underlying the coupled effects of confinement and crowding, we first consider the concentration regimes for the 14% and 28% dextran solutions that crowd the DNA molecules. These (w/w) dextran concentrations correspond to $\sim 5.5c^*$ (14%) and $\sim$13.5 c^* (28%) (Graessley, 1980), indicating substantial polymer overlap such that the solutions can be considered in the semidilute or concentrated regime. As described in the Introduction, previous studies have shown that solutions of 500 kDa dextran behave as semidilute solutions of overlapping (but unentangled) flexible polymers for concentrations ~5%–15%, and transition to the concentrated entanglement regime at ~15%–20% (Pinder et al., 2006; McCurdy et al., 1994). Across this entire concentration regime, when dissolved in water, dextran polymers assume ideal random coil configurations akin to flexible polymers in theta solvent conditions (Doi et al., 1988; McCurdy et al., 1994).

We note that the concentration of DNA in the solutions is much smaller than that of the dextran, such that we can assume that the overall solution concentration approximately matches the dextran concentration. We also can approximate each DNA molecule as being surrounded entirely by dextran polymers and their dynamics dictated solely by the crowding dextran. We acknowledge that the DNA concentration we use, comparable to its overlap concentration c^*_{DNA}, is higher than typical $c \ll c^*$ tracer concentrations. However, the DNA concentration is still >103 times lower than that of the dextran (0.0024% (w/w) vs 14% (w/w)), further justifying our simplification.

By approximating our systems as self-similar semidilute (14%) or entangled (28%) flexible polymer (dextran) solutions, we can compare our data to predictions for the scaling of diffusion coefficients of overlapping and entangled polymers with polymer concentration c. Firstly, the diffusion coefficient is predicted to scale with concentration as $D \sim c^{-x}$ where x is determined by the solvent conditions and concentration regime (Rubinstein and Colby, 2003). For unentangled but overlapping polymers, $x \simeq 1$ or $x \simeq 0.54$ for theta solvent or good solvent conditions, respectively. For entangled polymers (Robertson and Smith, 2007; Colby, 2010; Kulicke and Kniewske, 1984; Onogi et al., 1967), $x \simeq 7/3$ or $x \simeq 1.85$ for theta solvent or good solvent conditions. Of note, in the entangled regime, as polymer concentration increases, polymers that are in good solvent conditions often transition to theta solvent scaling as self-avoiding coils start to collapse (Colby, 2010).

To first check if the bulk dynamics of our system are consistent with these scaling relations, we compare the diffusion coefficients measured in bulk solutions of 14% and 28% dextran, $D_{B,14}/D_{B,28} \simeq 5.48 \pm 0.65$, to the

predicted scaling equation $(D_{B,14}/D_{B,28}) = (c_{14}/c_{28})^{-x} \sim 2^x$. Solving this equation yields $x \simeq 2.4 \pm 0.2$, which agrees remarkably well with the predicted theta solvent scaling $x \simeq 7/3 \simeq 2.33$ for entangled polymers, corroborating our assumption and previous reports that, at these concentrations, dextran is entangled and in theta solvent conditions.

Moreover, previous studies have reported that the viscosity of dextran solutions scales with concentration as $\eta \sim c^2$ in the semidilute regime (Pinder et al., 2006), similarly predicted for semidilute unentangled flexible polymers in theta solvents (Sabatie et al., 1988). This scaling exponent increases to ~3–4 in the entangled regime. Insofar as we can approximate that $D \sim \eta^{-1}$, these scaling laws are consistent with our bulk scaling of $x \simeq 2.4$. As the diffusion coefficients are measured in the two different regimes (semidilute unentangled versus entangled), we expect the scaling exponent to be intermediate between these values, which indeed it is.

Finally, previous studies examining particle diffusion in semidilute and entangled polymers have reported that in the limit where the tracer particle (DNA in our experiments) is larger than the crowding polymer size R_H, mesh size ξ, and entanglement tube radius a, that the particle diffusion coefficient scales with concentration as $x \simeq 4$. For intermediate-sized particles which are larger than the mesh size and coil size but smaller than the tube radius, $x \simeq 2.3$. For the unentangled regime (as for the 14% dextran solution), the tube radius is infinitely large such that the DNA can be considered in the intermediate regime ($x \simeq 2.3$), whereas at 28% dextran the DNA should be treated as in the large size limit in which $x \simeq 4$. This scaling behavior, in line with those described above for overlapping and entangled dextran solutions, further corroborates our physical description of crowding dextran solutions and their impact on the diffusion of the DNA tracers.

Now, to determine the mechanism driving the confinement-mediated slowing of DNA under these crowding conditions, we consider the volume excluded to the dextran near the lipid walls. Depletion of the dextran from a layer of thickness r would effectively increase the dextran concentration by decreasing the available volume. Namely, $c_{eff} = m/V_{eff} = 3m/4\pi(R - r)^3$ where m is polymer mass and R is the droplet radius. We postulate that the depletion layer that separates the dextran solution and lipid membrane should be comparable to the DNA coil size, i.e., $r \approx R_0$. Previous works have shown that dextran acts as a depletant for large DNA, causing it to compact, elongate, or swell to maximize available volume (Chapman et al., 2015; Zhang et al., 2009). This effect implies that the dextran polymers cannot penetrate the DNA coils (of size R_0) and would thus be excluded from their coil volume. Within this framework, we may also expect dextran polymers to crowd DNA to the lipid membrane surface, a typical interaction between small polymer depletants and dilute large polymers (Kulkarni et al., 1999; Kojima et al., 2006). We therefore expect that the DNA coil size dictates the depletion layer for the dextran which in turn increases the dextran concentration. In the absence of DNA, dextran would be depleted from the membrane surface by a layer of $\sim R_{H,dx}$, but because $R > R_0 \gg R_{H,dx}$, any surface-mediated depletion of the dextran would have a negligible effect on the effective dextran concentration.

As such, we combine the relations $r \approx R_0$ with $m = c_B V = (4\pi/3) c_B R^3$, where c_B is the bulk dextran concentration, to estimate a confinement-dependent effective dextran concentration of $c_{eff} = c_B[1 - (R_0/R)]^{-3}$. To determine R_0,we recall that in theta solvent conditions, polymer coils are described as ideal random walks, independent of concentration, such that R_0 depends on the number N of Kuhn lengths of size b, via the relation $R_0 \approx bN^{\nu} c^{-\beta}$ where $\nu \approx 0.5$ and $\beta = 0$ (Zimm, 1956; Doi et al., 1988; Colby, 2010). Conversely, in good solvent conditions, polymer coils are swollen and described by concentration-dependent self-avoiding random walks in which $\nu \approx 0.588$ and $\beta \simeq 1/8$ (Daoud et al., 1975; Nierlich et al., 1985; Rubinstein and Colby, 2003; Colby, 2010).

We now incorporate this expression into the scaling relations discussed above to phenomenologically couple the effects of crowding and confinement: $D/D_B = (c_{eff}/c_B)^{-x} = [1 - (R_0/R)]^{3x}$. We also recall $R_0 \sim c^{-\beta}$ from which we can approximate $R_{0,eff} = R_0(c_{eff}/c_B)^{-\beta} \simeq R_0[1 - (R_0/R)]^{3\beta}$ such that $D/D_B \simeq [1 - (R_0[1 - (R_0/R)]^{3\beta}/R)]^{3x}$.

For the 115 kbp linear DNA we use here, $b \simeq 100$ nm and $N \simeq 383$ such that $R_{0,\theta} \approx 1.96$ μm and $R_{0,G} \approx 3.30$ μm for theta solvent and good solvent conditions, respectively. While our buffer conditions are good solvent conditions for the DNA, we expect that the high degree of dextran-crowding, which screens hydrodynamic interactions and can lead to depletion-driven compaction (Gorczyca et al., 2015; Kojima et al., 2006; Zhang et al., 2009), would result in ideal random walk conformations akin to theta solvent conditions (Colby, 2010).

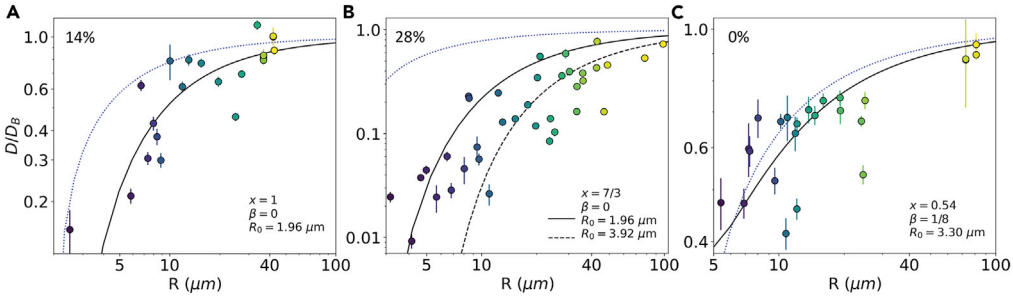

Figure 6. Depletion effects, polymer entanglements, and solvent conditions dictate how crowding amplifies confinement-induced slowing of DNA dynamics

Diffusion coefficients D of DNA confined in droplets, normalized by their respective values in bulk solution D_B can be described by the model $D/D_B \simeq 1 - (R_0/R)][1 - (R_0/R)][1 - (R_0/R)]^{3\beta}/R)]^{3x}$ (black curves) in which x, β and the DNA coil size R_0 depend on dextran entanglements and solvent conditions. The dotted line shows the prediction from Ref (Behrens et al., 2003) for increased hydrodynamic drag of particles near a confining surface.

(A) D/D_B for DNA in 14% dextran is well described by the model considering theta solvent conditions and semidilute unentangled dextran polymers. In this case $x \simeq 1$, $\beta = 0$, and $R_0 = R_{0,\theta} \approx 1.96$ μm.

(B) For the more concentrated 28% dextran solution, D/D_B of is also well described by theta solvent conditions but in the entanglement regime where $x \simeq 7/3$, $\beta = 0$, and $R_{0,\theta} \approx 1.96$ μm (solid black curve). Black dashed curve shows the prediction assuming 2-fold swelling of the DNA coil size, i.e., $R_0 = 2R_{0,\theta}$, which is applicable for dextran concentrations above ~20%.

(C) Without dextran crowding, the model fits D/D_B for semidilute unentangled DNA polymers in good solvent conditions, where $x \simeq 0.54$, $\beta = 1/8$, and $R_0 = R_{0,G} \simeq 3.30$ μm. Error bars represent the standard deviation of the distribution of individual $D(q)$ values computed for each q value.

Comparing our data to this model, we find that with 14% dextran crowding, the confinement-mediated decrease in diffusion coefficients agrees with the scaling for semidilute unentangled polymers in theta solvent conditions in which $x \simeq 1$, $\nu \simeq 0.5$, $\beta = 0$, and $R_{0,\theta} \approx 1.96$ μm (Figure 6A). This agreement is consistent with results of previous works that show that at this concentration, dextran solutions indeed behave as unentangled, semidilute solutions of flexible polymers. More importantly, it suggests that the confinement-mediated decrease in DNA diffusion may be explained by the increase in the effective dextran concentration resulting from the depletion layer formed by the DNA crowded to the membrane surface.

Within this framework, we expect the data for 28% dextran crowding to likewise be described by theta solvent models but follow scaling for the entangled regime. Indeed, Figure 6B shows that our data nicely follow the scaling for entangled polymers in theta solvent conditions in which $x \simeq 7/3$ (rather than 1), $\nu \simeq 0.5$, $\beta = 0$, and $R_{0,\theta} \approx 1.96$ μm (solid black line in Figure 6B). However, we note that a fair amount of the data, particularly for larger droplets, falls below the theoretical curve. To understand this effect, we turn to previous bulk measurements on DNA crowded by dextran, in which the DNA coil size was reported to swell nearly 2-fold for dextran concentrations $\gtrsim$ 20% (Gorczyca et al., 2015). If we take $R_{0,\theta} \rightarrow 2R_{0,\theta}$, the modified theoretical curve captures these slower than expected data (dashed line in Figure 6B), suggesting that similar swelling may be occurring here for sufficiently large droplets.

As a final check, to determine the validity of the models proposed above, we turn to the effect of confinement on DNA diffusion in the absence of dextran crowding (0%, Figure 6C). In this case, the polymer concentration to consider is that of the DNA, rather than dextran, such that we expect good solvent conditions and minimal polymer overlap ($c \approx c^*_{DNA}$). In this regime, $x \simeq 0.54$, $\nu \simeq 0.588$, $\beta \simeq 1/8$, and $R_{0,G} \simeq 3.30$ μm in the expression above for D/D_B. As shown, our data without crowders indeed align remarkably well with this prediction (black line in Figure 6C).

However, because there are no crowders to screen hydrodynamic interactions in this case, increased hydrodynamic drag from interactions with the lipid membrane may also contribute to the confinement-mediated decrease (Goldman et al., 1967). Previous studies examining the diffusion of particles near hard walls of confining slits, spheres, channels, and other geometries have shown that increased hydrodynamic drag near the surface slows the diffusion of the particles in a manner dependent on the size of the particle δ relative to its distance from the confining wall d (Lin et al., 2000; Pawar and Anderson, 1993;

Bevan and Prieve, 2000; Broersma, 1959; Zembrzycki et al., 2012; Kazoe and Yoda, 2011). Ref (Behrens et al., 2003) describes this reduced diffusion via the relation $D/D_B \simeq (6d^2 + 2\delta d)/(6d^2 + 9\delta d + 2\delta^2)$. Adopting the following equivalences: $\delta \simeq R_{0,G}$ and $d \simeq R$, we compare this prediction to our data (Figure 6). We find that for larger droplet sizes, the model we derive above describes the data more accurately than this confinement model, which does not account for polymer concentration. However, for very small droplets, $R \lesssim 3R_{0,G}$,the stronger decay of D with R for this model better captures our data trend, indicating that when the confinement size approaches the size of the DNA, surface interactions dominate over the effective increase in DNA concentration via depletion.

Importantly, the much larger drop in the diffusion coefficients in the presence of dextran crowders cannot be explained by the increased hydrodynamic drag, which leads to a ~3-fold decrease in DNA diffusion coefficients as R is reduced to ~5 μm, compared to a ~5-fold and ~100-fold decrease when crowded by 14% and 28% dextran solutions, respectively. At these high polymer concentrations, hydrodynamic interactions are typically screened, and, instead, the increase in the effective dextran concentration with decreasing R appears to dictate the slowing of the DNA dynamics.

In conclusion, the intracellular environment presents highly crowded and confined conditions which can significantly hamper the thermal motion of large macromolecules like DNA. While both crowding and confinement have been studied through experiments, simulations, and theory, how crowding and confinement collectively affect transport, particularly that of large macromolecules, has received considerably less attention. By using differential dynamic microscopy, we show how the synergistic effects of confinement and crowding can lead to subdiffusion of large macromolecules, independent of the details of the crowding and confinement conditions, as well as a substantial reduction in their diffusivity, even when the confinement size is well above the macromolecule size. In particular, the effective diffusion coefficient of DNA molecules in 28% dextran droplets decreases by more than an order of magnitude as the confining droplet radius decreases from ~100 to ~3 μm.

Our collective results, rather surprising given the weak confinement in our systems compared to the nanoscale confinement explored in many previous studies, are fully consistent with existing scaling models for how polymer diffusion and coil size vary with concentration in the regime of overlapping polymers. By recognizing that depletion effects at the droplet wall will increase the effective polymer concentration within the droplet above that of the bulk polymer concentration, we derive a scaling model that relates changes in DNA diffusion coefficients to changing droplet size. Notably, our model contains no free fitting parameters, and is able to accurately capture our observations across the entire range of droplet sizes and crowder concentrations that we examine.

The tunability of our experimental system, and generality of our DDM analyses and mathematical modeling, make our approaches and results broadly applicable to crowded and confined polymeric systems. More specifically, our results may prove valuable to understanding the results of myriad recent studies examining passive and active intracellular transport, many of which have pointed to the importance of both crowding and confinement on the observed dynamics (Chakraborty et al., 2022; Lin et al., 2016; Watanabe et al., 2020; Gomez-Navarro et al., 2020; Pereira de Souza et al., 2011; Dominak et al., 2010; Dominak and Keating, 2008). Finally, our specific results may shed light on intracellular processes that rely on the DNA transport such as transfection, replication, and gene therapy.

Limitations of the study

Here, we studied how the dynamics of DNA molecules are affected by crowding and confinement. The method of differential dynamic microscopy allowed us to quantify the ensemble averaged diffusion coefficients of DNA in droplets of various sizes and with different concentrations of dextran. However, this method does not allow us to determine the trajectories of individual DNA molecules nor their conformational dynamics. Future work could employ single particle tracking and conformational analysis which would allow us to determine, e.g., heterogeneity in the transport dynamics and how dynamics depend on the distance between the DNA and the droplet interface. Additional future work could probe how the dynamics of DNA within confined environments are affected by different types of crowders, such as dextran of different molecular weights, filamentous polymers, or mixtures of various crowders.

STAR★METHODS

Detailed methods are provided in the online version of this paper and include the following:

- KEY RESOURCES TABLE
- RESOURCE AVAILABILITY
  - Lead contact
  - Material availability
  - Data and code availability
- METHOD DETAILS
  - Sample preparation
  - Laser scanning confocal microscopy
  - Differential dynamics microscopy (DDM)

SUPPLEMENTAL INFORMATION

Supplemental information can be found online at https://doi.org/10.1016/j.isci.2022.105122.

ACKNOWLEDGMENTS

R.J.M. and R.M.R.A. acknowledge support from National Institutes of Health R15 Awards (R15GM123420, 2R15GM123420-02). R.M.R.A. acknowledges support from AFOSR (FA9550-21-1-0361).

AUTHOR CONTRIBUTIONS

M.S.A. developed protocols, designed experiments, collected and analyzed data, and wrote the paper; S.D. helped collect data and develop protocols; J.M. and K.C. developed protocols and prepared reagents; R.J.M. conceived, designed and guided the project, developed analysis code, analyzed and interpreted the data, and wrote the paper; R.M.R.A. conceived, designed, and guided the project, analyzed and interpreted the data, developed models, and wrote the paper.

DECLARATION OF INTERESTS

The authors declare no competing interests.

Received: August 4, 2022
Revised: August 27, 2022
Accepted: September 8, 2022
Published: October 21, 2022

REFERENCES

Armstrong, J.K., Wenby, R.B., Meiselman, H.J., and Fisher, T.C. (2004). The hydrodynamic radii of macromolecules and their effect on red blood cell aggregation. Biophys. J. *87*, 4259–4270.

Balducci, A., Mao, P., Han, J., and Doyle, P.S. (2006). Double-stranded DNA diffusion in slitlike nanochannels. Macromolecules *39*, 6273–6281.

Banks, D.S., and Fradin, C. (2005). Anomalous diffusion of proteins due to molecular crowding. Biophys. J. *89*, 2960–2971.

Behrens, S.H., Plewa, J., and Grier, D.G. (2003). Measuring a colloidal particle's interaction with a flat surface under nonequilibrium conditions. Eur. Phys. J. E Soft Matter *10*, 115–121.

Bevan, M.A., and Prieve, D.C. (2000). Hindered diffusion of colloidal particles very near to a wall: revisited. J. Chem. Phys. *113*, 1228–1236.

Bonthuis, D.J., Meyer, C., Stein, D., and Dekker, C. (2008). Conformation and dynamics of DNA confined in slitlike nanofluidic channels. Phys. Rev. Lett. *101*, 108303.

Broersma, S. (1959). Diffusion and viscosity in a spherical cavity. J. Chem. Phys. *30*, 707–717.

Bucciarelli, S., Myung, J.S., Farago, B., Das, S., Vliegenthart, G.A., Holderer, O., Winkler, R.G., Schurtenberger, P., Gompper, G., and Stradner, A. (2016). Dramatic influence of patchy attractions on short-time protein diffusion under crowded conditions. Sci. Adv. *2*, e1601432.

Cerbino, R., and Trappe, V. (2008). Differential dynamic microscopy: probing wave vector dependent dynamics with a microscope. Phys. Rev. Lett. *100*, 188102.

Cerbino, R., Giavazzi, F., and Helgeson, M.E. (2022). Differential dynamic microscopy for the characterization of polymer systems. J. Polym. Sci. *60*, 1079–1089.

Cerbino, R., Piotti, D., Buscaglia, M., and Giavazzi, F. (2017). Dark field differential dynamic microscopy enables accurate characterization of the roto-translational dynamics of bacteria and colloidal clusters. J. Phys. Condens. Matter *30*, 025901.

Chakraborty, R., Maiti, A., Sharma, N., and Dey, K.K. (2022). Active Matter Dynamics in Confined Microfluidic Environments. Micro/Nanofluidics and Lab-on-Chip Based Emerging Technologies for Biomedical and Translational Research Applications-Part A, p. 245.

Chapman, C.D., Gorczyca, S., and Robertson-Anderson, R.M. (2015). Crowding induces complex ergodic diffusion and dynamic elongation of large DNA molecules. Biophys. J. *108*, 1220–1228.

Chen, Y.-L., Graham, M.D., de Pablo, J.J., Randall, G.C., Gupta, M., and Doyle, P.S. (2004). Conformation and dynamics of single DNA molecules in parallel-plate slit microchannels. Phys. Rev. E Stat. Nonlin. Soft Matter Phys. *70*, 060901.

Colby, R.H. (2010). Structure and linear viscoelasticity of flexible polymer solutions: comparison of polyelectrolyte and neutral polymer solutions. Rheol. Acta *49*, 425–442.

Daoud, M., Cotton, J.P., Farnoux, B., Jannink, G., Sarma, G., Benoit, H., Duplessix, C., Picot, C., and de Gennes, P.G. (1975). Solutions of flexible polymers. Neutron experiments and interpretation. Macromolecules *8*, 804–818.

De Gennes, P.-G., and Gennes, P.-G. (1979). Scaling Concepts in Polymer Physics (Cornell University Press).

Dix, J.A., and Verkman, A.S. (2008). Crowding effects on diffusion in solutions and cells. Annu. Rev. Biophys. *37*, 247–263.

Doi, M., Edwards, S.F., and Edwards, S.F. (1988). The Theory of Polymer Dynamics (Oxford University Press).

Dominak, L.M., and Keating, C.D. (2008). Macromolecular crowding improves polymer encapsulation within giant lipid vesicles. Langmuir *24*, 13565–13571.

Dominak, L.M., Omiatek, D.M., Gundermann, E.L., Heien, M.L., and Keating, C.D. (2010). Polymeric crowding agents improve passive biomacromolecule encapsulation in lipid vesicles. Langmuir *26*, 13195–13200.

Drechsler, M., Giavazzi, F., Cerbino, R., and Palacios, I.M. (2017). Active diffusion and advection in Drosophila oocytes result from the interplay of actin and microtubules. Nat. Commun. *8*, 1520–1611.

Elowitz, M.B., Surette, M.G., Wolf, P.-E., Stock, J.B., and Leibler, S. (1999). Protein mobility in the cytoplasm of Escherichia coli. J. Bacteriol. *181*, 197–203.

Feriani, L., Juenet, M., Fowler, C.J., Bruot, N., Chioccioli, M., Holland, S.M., Bryant, C.E., and Cicuta, P. (2017). Assessing the collective dynamics of motile cilia in cultures of human airway cells by multiscale DDM. Biophys. J. *113*, 109–119.

Giavazzi, F., Brogioli, D., Trappe, V., Bellini, T., and Cerbino, R. (2009). Scattering information obtained by optical microscopy: differential dynamic microscopy and beyond. Phys. Rev. E Stat. Nonlin. Soft Matter Phys. *80*, 031403.

Giavazzi, F., Edera, P., Lu, P.J., and Cerbino, R. (2017). Image windowing mitigates edge effects in Differential Dynamic Microscopy. Eur. Phys. J. E Soft Matter *40*, 97–99.

Giavazzi, F., Trappe, V., and Cerbino, R. (2020). Multiple dynamic regimes in a coarsening foam. J. Phys. Condens. Matter *33*, 024002.

Golding, I., and Cox, E.C. (2006). Physical nature of bacterial cytoplasm. Phys. Rev. Lett. *96*, 098102.

Goldman, A.J., Cox, R.G., and Brenner, H. (1967). Slow viscous motion of a sphere parallel to a plane wall—I Motion through a quiescent fluid. Chemical engineering science *22*, 637–651.

Gomez-Navarro, N., Melero, A., Li, X.-H., Boulanger, J., Kukulski, W., and Miller, E.A. (2020). Cargo crowding contributes to sorting stringency in COPII vesicles. J. Cell Biol. *219*, e201806038.

Gorczyca, S.M., Chapman, C.D., and Robertson-Anderson, R.M. (2015). Universal scaling of crowding-induced DNA mobility is coupled with topology-dependent molecular compaction and elongation. Soft Matter *11*, 7762–7768.

Graessley, W. (1980). Polymer chain dimensions and the dependence of viscoelastic properties on concentration, molecular weight and solvent power. Polymer *21*, 258–262.

Guan, J., Wang, B., and Granick, S. (2014). Even hard-sphere colloidal suspensions display Fickian yet non-Gaussian diffusion. ACS Nano *8*, 3331–3336.

Guo, H., Bourret, G., Lennox, R.B., Sutton, M., Harden, J.L., and Leheny, R.L. (2012). Entanglement-controlled subdiffusion of nanoparticles within concentrated polymer solutions. Phys. Rev. Lett. *109*, 055901.

Harusawa, K., Watanabe, C., Kobori, Y., Tomita, K., Kitamura, A., Kinjo, M., and Yanagisawa, M. (2020). Membrane surface modulates slow diffusion in small crowded droplets. Langmuir *37*, 437–444.

He, K., Babaye Khorasani, F., Retterer, S.T., Thomas, D.K., Conrad, J.C., and Krishnamoorti, R. (2013). Diffusive dynamics of nanoparticles in arrays of nanoposts. ACS Nano *7*, 5122–5130.

He, Y., Burov, S., Metzler, R., and Barkai, E. (2008). Random time-scale invariant diffusion and transport coefficients. Phys. Rev. Lett. *101*, 058101.

Helenius, J., Brouhard, G., Kalaidzidis, Y., Diez, S., and Howard, J. (2006). The depolymerizing kinesin MCAK uses lattice diffusion to rapidly target microtubule ends. Nature *441*, 115–119.

Hitimana, E., Roopnarine, B.K., and Morozova, S. (2022). Diffusive dynamics of charged nanoparticles in convex lens-induced confinement. Soft Matter *18*, 832–840.

Höfling, F., and Franosch, T. (2013). Anomalous transport in the crowded world of biological cells. Rep. Prog. Phys. *76*, 046602.

Jacob, J.D.C., He, K., Retterer, S.T., Krishnamoorti, R., and Conrad, J.C. (2015). Diffusive dynamics of nanoparticles in ultra-confined media. Soft Matter *11*, 7515–7524.

Jones, J.J., van der Maarel, J.R.C., and Doyle, P.S. (2011). Effect of nanochannel geometry on DNA structure in the presence of macromolecular crowding agent. Nano Lett. *11*, 5047–5053.

Junker, N.O., Vaghefikia, F., Albarghash, A., Höfig, H., Kempe, D., Walter, J., Otten, J., Pohl, M., Katranidis, A., Wiegand, S., and Fitter, J. (2019). Impact of molecular crowding on translational mobility and conformational properties of biological macromolecules. J. Phys. Chem. B *123*, 4477–4486.

Kato, A., Shindo, E., Sakaue, T., Tsuji, A., and Yoshikawa, K. (2009). Conformational transition of giant DNA in a confined space surrounded by a phospholipid membrane. Biophys. J. *97*, 1678–1686.

Kazoe, Y., and Yoda, M. (2011). Measurements of the near-wall hindered diffusion of colloidal particles in the presence of an electric field. Appl. Phys. Lett. *99*, 124104.

Kohli, I., and Mukhopadhyay, A. (2012). Diffusion of nanoparticles in semidilute polymer solutions: effect of different length scales. Macromolecules *45*, 6143–6149.

Kojima, M., Kubo, K., and Yoshikawa, K. (2006). Elongation/compaction of giant DNA caused by depletion interaction with a flexible polymer. J. Chem. Phys. *124*, 024902.

Konopka, M.C., Shkel, I.A., Cayley, S., Record, M.T., and Weisshaar, J.C. (2006). Crowding and confinement effects on protein diffusion *in vivo*. J. Bacteriol. *188*, 6115–6123.

Kulicke, W.-M., and Kniewske, R. (1984). The shear viscosity dependence on concentration, molecular weight, and shear rate of polystyrene solutions. Rheol. Acta *23*, 75–83.

Kulkarni, A.M., Chatterjee, A.P., Schweizer, K.S., and Zukoski, C.F. (1999). Depletion interactions in the protein limit: effects of polymer density fluctuations. Phys. Rev. Lett. *83*, 4554–4557.

Kwon, G., Sung, B.J., and Yethiraj, A. (2014). Dynamics in crowded environments: is non-Gaussian Brownian diffusion normal? J. Phys. Chem. B *118*, 8128–8134.

Laib, S., Robertson, R.M., and Smith, D.E. (2006). Preparation and characterization of a set of linear DNA molecules for polymer physics and rheology studies. Macromolecules *39*, 4115–4119.

Lin, B., Yu, J., and Rice, S.A. (2000). Direct measurements of constrained Brownian motion of an isolated sphere between two walls. Phys. Rev. E Stat. Phys. Plasmas Fluids Relat. Interdiscip. Topics *62*, 3909–3919.

Lin, C., Schuster, M., Guimaraes, S.C., Ashwin, P., Schrader, M., Metz, J., Hacker, C., Gurr, S.J., and Steinberg, G. (2016). Active diffusion and microtubule-based transport oppose myosin forces to position organelles in cells. Nat. Commun. *7*, 11814.

Lu, P.J., Giavazzi, F., Angelini, T.E., Zaccarelli, E., Jargstorff, F., Schofield, A.B., Wilking, J.N., Romanowsky, M.B., Weitz, D.A., and Cerbino, R. (2012). Characterizing concentrated, multiply scattering, and actively driven fluorescent systems with confocal differential dynamic microscopy. Phys. Rev. Lett. *108*, 218103.

Lukacs, G.L., Haggie, P., Seksek, O., Lechardeur, D., Freedman, N., and Verkman, A.S. (2000). Size-dependent DNA mobility in cytoplasm and nucleus. J. Biol. Chem. *275*, 1625–1629.

Martinez, V.A., Besseling, R., Croze, O.A., Tailleur, J., Reufer, M., Schwarz-Linek, J., Wilson, L.G., Bees, M.A., and Poon, W.C.K. (2012). Differential dynamic microscopy: a high-throughput method for characterizing the motility of microorganisms. Biophys. J. *103*, 1637–1647.

McCurdy, R., Goff, H., Stanley, D., and Stone, A. (1994). Rheological properties of dextran related to food applications. Food Hydrocolloids *8*, 609–623.

McGuffee, S.R., and Elcock, A.H. (2010). Diffusion, crowding & protein stability in a dynamic molecular model of the bacterial cytoplasm. PLoS Comput. Biol. *6*, e1000694.

Metzler, R., Jeon, J.-H., and Cherstvy, A.G. (2016). Non-Brownian diffusion in lipid membranes: experiments and simulations. Biochim. Biophys. Acta *1858*, 2451–2467.

Miyoshi, D., and Sugimoto, N. (2008). Molecular crowding effects on structure and stability of DNA. Biochimie *90*, 1040–1051.

Morrin, G.T., Kienle, D.F., and Schwartz, D.K. (2021). Diffusion of short semiflexible DNA polymer chains in strong and moderate confinement. ACS Macro Lett. *10*, 1191–1195.

Nakano, S.-I., Miyoshi, D., and Sugimoto, N. (2014). Effects of molecular crowding on the structures, interactions, and functions of nucleic acids. Chem. Rev. *114*, 2733–2758.

Nierlich, M., Boue, F., Lapp, A., and Oberthür, R. (1985). Characteristic lengths and the structure of salt free polyelectrolyte solutions. A small angle neutron scattering study. Colloid Polym. Sci. *263*, 955–964.

Onogi, S., Kimura, S., Kato, T., Masuda, T., and Miyanaga, N. (1967). Effects of molecular weight and concentration on flow properties of concentrated polymer solutions. Journal of Polymer Science Part C: Polymer Symposia (Wiley Online Library), pp. 381–406.

Pawar, Y., and Anderson, J.L. (1993). Hindered diffusion in slit pores: an analytical result. Ind. Eng. Chem. Res. *32*, 743–746.

Pereira De Souza, T., Steiniger, F., Stano, P., Fahr, A., and Luisi, P.L. (2011). Spontaneous crowding of ribosomes and proteins inside vesicles: a possible mechanism for the origin of cell metabolism. Chembiochem *12*, 2325–2330.

Persson, F., Utko, P., Reisner, W., Larsen, N.B., and Kristensen, A. (2009). Confinement spectroscopy: probing single DNA molecules with tapered nanochannels. Nano Lett. *9*, 1382–1385.

Pinder, D., Swanson, A., Hebraud, P., and Hemar, Y. (2006). Micro-rheological investigation of dextran solutions using diffusing wave spectroscopy. Food Hydrocolloids *20*, 240–244.

Polanowski, P., and Sikorski, A. (2016). Simulation of molecular transport in systems containing Mobile obstacles. J. Phys. Chem. B *120*, 7529–7537.

Regan, K., Wulstein, D., Rasmussen, H., Mcgorty, R., and Robertson-Anderson, R.M. (2019). Bridging the spatiotemporal scales of macromolecular transport in crowded biomimetic systems. Soft Matter *15*, 1200–1209.

Reisner, W., Morton, K.J., Riehn, R., Wang, Y.M., Yu, Z., Rosen, M., Sturm, J.C., Chou, S.Y., Frey, E., and Austin, R.H. (2005). Statics and dynamics of single DNA molecules confined in nanochannels. Phys. Rev. Lett. *94*, 196101.

Robertson, R.M., and Smith, D.E. (2007). Direct measurement of the confining forces imposed on a single molecule in a concentrated solution of circular polymers. Macromolecules *40*, 8737–8741.

Robertson, R.M., Laib, S., and Smith, D.E. (2006). Diffusion of isolated DNA molecules: dependence on length and topology. Proc. Natl. Acad. Sci. USA *103*, 7310–7314.

Roosen-Runge, F., Hennig, M., Zhang, F., Jacobs, R.M.J., Sztucki, M., Schober, H., Seydel, T., and Schreiber, F. (2011). Protein self-diffusion in crowded solutions. Proc. Natl. Acad. Sci. USA. *108*, 11815–11820.

Rubinstein, M., and Colby, R.H. (2003). Polymer Physics (Oxford University Press).

Sabatié, J., Choplin, L., Doublier, J., Arul, J., Paul, F., and Monsan, P. (1988). Rheology of native dextrans in relation to their primary structure. Carbohydr. Polym. *9*, 287–299.

Senti, F.R., Hellman, N.N., Ludwig, N.H., Babcock, G.E., Tobin, R., Glass, C.A., and Lamberts, B.L. (1955). Viscosity, sedimentation, and light-scattering properties of fraction of an acid-hydrolyzed dextran. J. Polym. Sci. *17*, 527–546.

Skóra, T., Vaghefikia, F., Fitter, J., and Kondrat, S. (2020). Macromolecular crowding: how shape and interactions affect diffusion. J. Phys. Chem. B *124*, 7537–7543.

Szymanski, J., and Weiss, M. (2009). Elucidating the origin of anomalous diffusion in crowded fluids. Phys. Rev. Lett. *103*, 038102.

Tan, C., Saurabh, S., Bruchez, M.P., Schwartz, R., and Leduc, P. (2013). Molecular crowding shapes gene expression in synthetic cellular nanosystems. Nat. Nanotechnol. *8*, 602–608.

Tang, J., Levy, S.L., Trahan, D.W., Jones, J.J., Craighead, H.G., and Doyle, P.S. (2010). Revisiting the conformation and dynamics of DNA in slitlike confinement. Macromolecules *43*, 7368–7377.

Verwei, H.N., Lee, G., Leech, G., Petitjean, I.I., Koenderink, G.H., Robertson-Anderson, R.M., and Mcgorty, R.J. (2022). Quantifying cytoskeleton dynamics using differential dynamic microscopy. JoVE, e63931.

Watanabe, C., Kobori, Y., Yamamoto, J., Kinjo, M., and Yanagisawa, M. (2020). Quantitative analysis of membrane surface and small confinement effects on molecular diffusion. J. Phys. Chem. B *124*, 1090–1098.

Weiss, M. (2014). Crowding, diffusion, and biochemical reactions. Int. Rev. Cell Mol. Biol. *307*, 383–417.

Weiss, M., Elsner, M., Kartberg, F., and Nilsson, T. (2004). Anomalous subdiffusion is a measure for cytoplasmic crowding in living cells. Biophys. J. *87*, 3518–3524.

Zembrzycki, K., Błoński, S., and Kowalewski, T. (2012). Analysis of wall effect on the process of diffusion of nanoparticles in a microchannel. J. Phys. Conf. Ser. 012014.

Zhang, C., Shao, P.G., Van Kan, J.A., and van der Maarel, J.R.C. (2009). Macromolecular crowding induced elongation and compaction of single DNA molecules confined in a nanochannel. Proc. Natl. Acad. Sci. USA *106*, 16651–16656.

Zhou, H.-X. (2013). Influence of crowded cellular environments on protein folding, binding, and oligomerization: biological consequences and potentials of atomistic modeling. FEBS Lett. *587*, 1053–1061.

Zhou, H.-X., Rivas, G., and Minton, A.P. (2008). Macromolecular crowding and confinement: biochemical, biophysical, and potential physiological consequences. Annu. Rev. Biophys. *37*, 375–397.

Zimm, B.H. (1956). Dynamics of polymer molecules in dilute solution: viscoelasticity, flow birefringence and dielectric loss. J. Chem. Phys. *24*, 269–278.

STAR★METHODS

KEY RESOURCES TABLE

REAGENT or RESOURCE	SOURCE	IDENTIFIER
Biological samples		
DNA	Robertson-Anderson Lab	http://www.biospotlab.com/
Chemicals, peptides, and recombinant proteins		
Dextran	Fisher BioReagents	Cat#18-602-091; CAS: 9004-54-0
Mineral oil	Acros Organics	Cat#AC415080060; CAS: 8042-47-5
MFP488 nucleic acid labeling reagent	Mirus, Lable IT Nucleic Acid Labeling Kit	MFP488
DOPE	Avanti Polar Lipids	CAS: 4004-05-1
Egg PC	Avanti Polar Lipids	CAS: 97281-44-2
PEG5k PE	Avanti Polar Lipids	CAS: 474922-84-4
Dimethyldichlorosilane	Acros Organics	Cat#AC430881000; CAS: 75-78-5
Software and algorithms		
Differential dynamics microscopy (DDM)	Verwei et al., 2022	https://doi.org/10.5281/zenodo.6626403
Python	Python Software Foundation	http://www.python.org/
ImageJ	National Institutes of Health	https://imagej.nih.gov/ij/

RESOURCE AVAILABILITY

Lead contact

Further information and requests for resources should be directed to and will be fulfilled by the lead contact, Rae M. Robertson-Anderson.

Material availability

This study did not generate new unique reagents.

Data and code availability

- Microscopy data reported in this paper will be shared by the lead contact upon request.
- Experimental data are analyzed using a custom written Python code. Diffusion coefficients are calculated from their definition in the text and their mean value and standard deviations are used in the figures. The statistical and analysis detail can be found in the figure captions and methods details. All original code has been deposited at Zenodo and is publicly available as of the date of publication. DOIs are listed in the key resources table.
- Any additional information required to reanalyze the data reported in this paper is available from the lead contact upon request.

METHOD DETAILS

Sample preparation

To create *in vitro* crowded environments, we use 500 kDa dextran (Fisher BioReagents BP1580-100) with a hydrodynamics radius of $R_H \simeq 16$ nm (Senti et al., 1955). An aqueous stock solution of dextran is prepared at a concentration of 40% (w/w) in TE10 buffer (10 mM Tris-HCl, 1 mM EDTA, 10 mM NaCl), which is further diluted for experiments which we perform at 28% (w/w) and 14% (w/w) dextran.

Double-stranded linear DNA ($L = 115$ kbp $\simeq 39$ μm, $R_0 \simeq 2$ μ m) is prepared, as described previously (Laib et al., 2006), via replication of bacterial artificial chromosomes in *E. coli*, followed by extraction, purification, and restriction endonuclease digestion to convert supercoiled DNA to linear topology. To image DNA for

analysis, we fluorescent-label DNA molecules with MFP488 nucleic acid labeling reagent (Mirus, Lable IT Nucleic Acid Labeling Kit, MFP488) using modified manufacturer protocols . For experiments, labeled DNA was diluted to 0.025 mg/mL in (1) TE10 buffer, (2) 14% dextran in TE10 or (3) 28% dextran in TE10. To reduce photobleaching, an oxygen scavenging solution (45 μg/mL glucose, 43 μg/mL glucose oxidase, and 7 μg/mL catalase) is added to the sample.

To form stable aqueous droplets in oil, we first prepare a lipid/oil solution. Our lipids include 1, 2-dioleoyl-sn-glycero-3-phosphoethanolamine (DOPE), L-α-phosphatidylcholine (Egg PC), and 1,2-dipalmitoyl-sn-glycro-3-phosphoethanolamine-N-[methoxy(polyethylene glycol)-5000] (PEG5k PE) from Avanti Polar Lipids. We dissolve 1.4 mg/mL DOPE, 0.5 mg/mL Egg PC, and 0.1 mg/mL PEG5k-PE in mineral oil (Acros Organics), and add the lipid-oil mixture to the DNA solution at an oil:water volume ratio of 10:1. We mix the sample by quickly pipetting up and down for ~10 s to form a water-oil emulsion. These methods result in spherical droplets of radius $R \simeq 3 - 100$ μm. We pipet the droplet solution into a sample chamber made of a microscope slide and coverslip separated by ~0.1 mm with double-sided tape and sealed with epoxy. We silanize the cover glass as described previously (Helenius et al., 2006) to prevent droplets from wetting the glass.

Laser scanning confocal microscopy

To image the labeled DNA molecules in droplets, we use a Nikon A1R laser scanning confocal microscope with a 60×1.4 NA oil immersion objective, 488 nm laser and 488/525 nm excitation/emission filters. We collect 2000-frame time-series of 512 × 512 pixel images at frame rates of 1, 2, and 33 fps for 28% dextran, 14% dextran, and 0% dextran, respectively.

Differential dynamics microscopy (DDM)

From the collected time-series of images, $I(\mathbf{x};t)$, we compute the image differences $\Delta I(\mathbf{x},t,\Delta t) = I(\mathbf{x},t+\Delta t) - I(\mathbf{x},t)$ for a range of lag times, Δt. For a given lag time, the spatial Fourier power spectra of image differences are computed using a fast Fourier transformation (FFT) routine and averaged together. This algorithm results in an image structure function (Cerbino and Trappe, 2008):

$$D(\mathbf{q},\Delta t) = \left|\Delta\widehat{I}(\mathbf{q},t,\Delta t)\right|_t^2 \qquad \text{(Equation 1)}$$

where, $\widehat{I}(\mathbf{q},t) = (1/2\pi)\iint d\mathbf{x} I(\mathbf{x},t)e^{-j\mathbf{q}\cdot\mathbf{x}}$ and $\mathbf{q} = (q_x, q_y)$ is the two-dimensional scattering wavevector. This image structure function is related to the intermediate scattering function (ISF), $f(\mathbf{q},\Delta t)$, according to the equation

$$D(\mathbf{q},\Delta t) = A(\mathbf{q})\left[1 - f(\mathbf{q},\Delta t)\right] + B(\mathbf{q}) \qquad \text{(Equation 2)}$$

where $B(q)$ is related to the camera noise and $A(q)$ is an amplitude term that contains details about the imaging system and static scattering properties of the sample (Giavazzi et al., 2017; Cerbino and Trappe, 2008). The ISF, $f(\mathbf{q},\Delta t)$, is the cumulative probability that displacements of an image element over lag time Δt will be within a length scale $\sim 1/q$. For stochastic processes that lose their memory over sufficiently long times, $f(\mathbf{q},\Delta t)$ will decay to zero. The functional form of the ISF depends on the system dynamics. Here, we consider isotropic samples where the image structure function $D(\mathbf{q},\Delta t)$ is azimuthally isotropic in the $\mathbf{q}$ plane. This isotropy allows us to perform azimuthal averages to yield $D(q,\Delta t)$ with the magnitude of the wavevector $q = \sqrt{q_x^2 + q_y^2}$ (Cerbino and Trappe, 2008; Giavazzi et al., 2009). To characterize anomalous diffusion, we consider a stretched exponential model to describe the image structure function (He et al., 2013; Jacob et al., 2015):

$$D(q,\Delta t) = A(q)\left[1 - \exp\left\{-\left(\frac{\Delta t}{\tau(q)}\right)^{s(q)}\right\}\right] + B(q) \qquad \text{(Equation 3)}$$

where $\tau(q)$ is a decay time and $s(q)$ is a stretching exponent. We extract $A(q)$, $B(q)$, $\tau(q)$, and $s(q)$ using a nonlinear least-squares fitting of the image structure function for each wavevector q.

One can also extract $f(\mathbf{q},\Delta t)$ from the computed image structure function by determining the parameters $A(q)$ and $B(q)$ without fitting to any function. To estimate $A(q)$ and $B(q)$, we compute the time-averaged

power spectrum of the image series, $|\widehat{I}(q,t)|^2 = (A(q) + B(q))/2$ (Cerbino et al., 2017; Giavazzi et al., 2020). In most experimental cases the noise term $B(q)$ is practically q-independent. Since $A(q \to \infty) = 0$ (Cerbino et al., 2022), we estimate the magnitude of B as the high-q limit of $2|\widehat{I}(q,t)|^2$. Once $A(q)$ and B are known, we extract the ISF from Equation (2) as $f(q,\Delta t) = 1 - (D(q,\Delta t) - B)/A(q)$.

We use custom written Python code to perform each step of the DDM analysis described above (Verwei et al., 2022).